


Image-quality characteristics in the longitudinal direction from different image-reconstruction algorithms during single-rotation volume acquisition on head computed tomography: A phantom study

Acta Radiologica Open
12(4) 1–10
© The Author(s) 2023
Article reuse guidelines:
sagepub.com/journals-permissions
DOI: 10.1177/20584601231168986
journals.sagepub.com/home/arr


Ryo Watanabe¹ , Ayako Zensho¹, Yoshitaka Ohishi¹ and Yoshinori Funama² 

Abstract

Background: A multi detector computed tomography (CT) scanner with wide-area coverage enables whole-brain volumetric scanning in a single rotation.

Purpose: To investigate variations in image-quality characteristics in the longitudinal direction for different image-reconstruction algorithms and strengths with phantoms.

Material and methods: Single-rotation volume scans were performed on a 320-row multidetector CT volume scanner using three types of phantoms. Tube current was set to 200 mA (standard dose) and 50 mA (low dose). All images were reconstructed with filtered back projection (FBP), mild and strong levels with hybrid iterative reconstruction (HIR), and model-based IR (MBIR). Computed tomography numbers, image noise, noise power spectrum (NPS), task-based transfer function (TTF), and visual spatial resolution were used to evaluate uniformity of image quality in the longitudinal direction (Z-axis).

Results: The MBIR images showed smaller variation in CT numbers in the Z-axis. The difference in the highest and lowest CT numbers was smaller (5.0 Hounsfield units [HU]) for MBIR than for FBP (6.6 HU) and HIR (6.8 HU). The variations in image noise were the smallest for strong MBIR and the largest for FBP. The low-frequency component at NPS_{0.2} was lower for strong MBIR than for other algorithms. The high-frequency component at NPS_{0.8} was low in all reconstructions. For MBIR, the image resolution and TTFs were higher in the outer portion than in the center.

Conclusion: Model-based IR is the optimal image-reconstruction algorithm for single-volume scan of spherical subjects owing to its high in-plane resolution and uniformity of CT numbers, image noise, and NPS in the Z-axis.

Keywords

Head computed tomography, single-rotation volume scan, reconstruction algorithm, image quality, longitudinal direction

Received 4 November 2022; accepted 23 March 2023

¹Department of Radiology, Hospital of the University of Occupational and Environmental Health, Kitakyushu, Japan

²Department of Medical Radiation Sciences, Faculty of Life Sciences, Kumamoto University, Kumamoto, Japan

Introduction

A multi detector computed tomography (CT) scanner with wide-area coverage enables volumetric axial scanning of the whole heart and brain in a single-gantry rotation. The

Corresponding author:

Ryo Watanabe, Department of Radiology, Hospital of the University of Occupational and Environmental Health, Iseigaoka 1-1, Yahatanishi-Ku, Kitakyushu 807-8555, Japan.

Email: byonnabe@clnc.uoeh-u.ac.jp



Creative Commons Non Commercial CC BY-NC: This article is distributed under the terms of the Creative Commons Attribution-NonCommercial 4.0 License (<https://creativecommons.org/licenses/by-nc/4.0/>) which permits non-commercial use, reproduction and distribution of the work without further permission provided the original work is attributed as specified on the SAGE and Open Access pages (<https://us.sagepub.com/en-us/nam/open-access-at-sage>).

usefulness of single-rotation volume scanning within a short time in CT angiography has been reported for the head in pediatric patients and for cerebral vessels and coronary arteries.^{1–6} Volume scanning is also used in perfusion CT and four-dimensional CT in which the same area is imaged in a time series by successive single-rotation volume acquisition.^{2,7–9}

When performing a single-rotation volume scan, a fixed radiation dose is used in whole-head CT because automatic exposure control is not applicable. Therefore, the incident radiation dose to the detector varies in the longitudinal direction owing to differences in the thickness of different parts of the head, such as at the basal ganglia and parietal levels. Consequently, noise distribution is not uniform for all slice levels from caudal to cranial sections of the head. Iterative reconstruction (IR) algorithms, such as hybrid iterative reconstruction (HIR) and model-based iterative reconstruction (MBIR), show nonlinear image noise reduction and improved image quality.^{10–19} Therefore, we believe that the use of IR algorithms reduces the inhomogeneity of image noise in the longitudinal direction obtained by single-rotation volume scans relative to that obtained by the conventional image-reconstruction algorithm with filtered back projection (FBP). However, researchers have reported that IR can alter image-quality characteristics, such as spatial resolution and noise texture, depending on the intensity of the nonlinear processing and the object.^{12,15–18}

This study aimed to investigate the variations in image-quality characteristics, such as image noise and spatial resolution, in the longitudinal direction for different image-reconstruction algorithms and strengths in whole-head CT with single-rotation volume scanning using a 320-detector row CT scanner.

Materials and methods

Phantom

Three self-made acrylic spherical phantoms (diameter: 200 mm, acrylic wall thickness: 2.5 mm, sphere lumen diameter: 195 mm) in a human head shape were used in our study (water uniform sphere phantom, [Figure 1\(a\)](#); Delrin[®] cylinder sphere phantom, [Figure 1\(b\)](#); and comb sphere phantom, [Figure 1\(c\)](#)). A Delrin[®] cylinder (diameter: 20 mm, length: 180 mm, CT number: 350 Hounsfield units [HU]) was inserted at the center portion of the Delrin[®] cylinder sphere phantom for assuming vessel enhancement on head CT angiography ([Figure 1\(b\)](#)). A comb sphere phantom consisting of a square wooden pillar fixed in the center of a water uniform sphere phantom and a polycarbonate comb (length: 180 mm, width: 30 mm, pitch: 1.5 mm) was placed on the square pillar ([Figure 1\(c\)](#)).

Scanning parameters and image reconstruction

All phantoms were fixed to a device for head imaging and placed in the center of rotation of the X-ray tube and detector. The Delrin[®] cylinder and comb were positioned such that the long axes were orthogonal to the slice. All scans were performed on a second-generation wide-volume 320-row multidetector CT (Aquilion ONE Vision Edition; Canon Medical Systems, Otawara, Japan) scanner with one-shot volume acquisition and no table movement. The scan parameters were as follows: tube voltage, 120 kV; gantry rotation speed, 1.0 s; detector configuration, 320 × 0.5 mm; scan and display field of view (FOV), 240 × 240 mm; slice thickness, 5.0 mm; and image matrix, 512 × 512. The tube current was set to 200 mA for the standard-dose scan and 50 mA for the low-dose scan. The image-noise level ranged from 3.0 to 5.0 HU for the standard-dose scan and from 6.0 to 10.0 HU for the low-dose scan. The CT scanning was repeated five times at the same position and under the same scan parameters. All images were reconstructed with FBP, HIR with two IR strengths (Adaptive Iterative Dose Reduction 3D: AIDR3D with mild and strong levels), and MBIR with two IR strengths (forward-projected MBIR Solution: FIRST Brain with mild and strong levels). The FBP and HIR algorithms used a brain standard reconstruction kernel (FC21).

Image analysis

CT numbers and image noises. To assess the CT number and image noise (standard deviation of the image pixel values) uniformity in the longitudinal direction, the CT number and image noise (standard deviation of the image pixel values) were calculated using regions of interest (ROIs) of 35 × 35 pixels at the center and four other locations of the water uniform spherical phantom ([Figure 1\(a\)](#)). The five ROIs in each slice location were calculated as the mean value obtained from 25 consecutive axial images (five ROIs × five repeated scans) using ImageJ software (National Institutes of Health).²⁰ The same measurements were repeated in the longitudinal direction (table position, −70 to +70 mm; 29 consecutive axial images). The CT number and image noise were obtained for FBP images and mild and strong HIR and MBIR images.

Noise power spectrum (NPS). The NPS was measured at ROIs of 35 × 35 pixels at the center and four other locations using imQuest software (Duke University, Durham, 2018) ([Figure 1\(a\)](#)).^{21–23} The NPS was measured from the mean value of 25 measurement points (five ROIs × five repeated scans) in each slice level and repeated on 29 consecutive axial images in the longitudinal direction. The NPS was obtained for FBP images and mild and strong HIR and MBIR images. Finally, NPS values at 0.2 cycle/mm

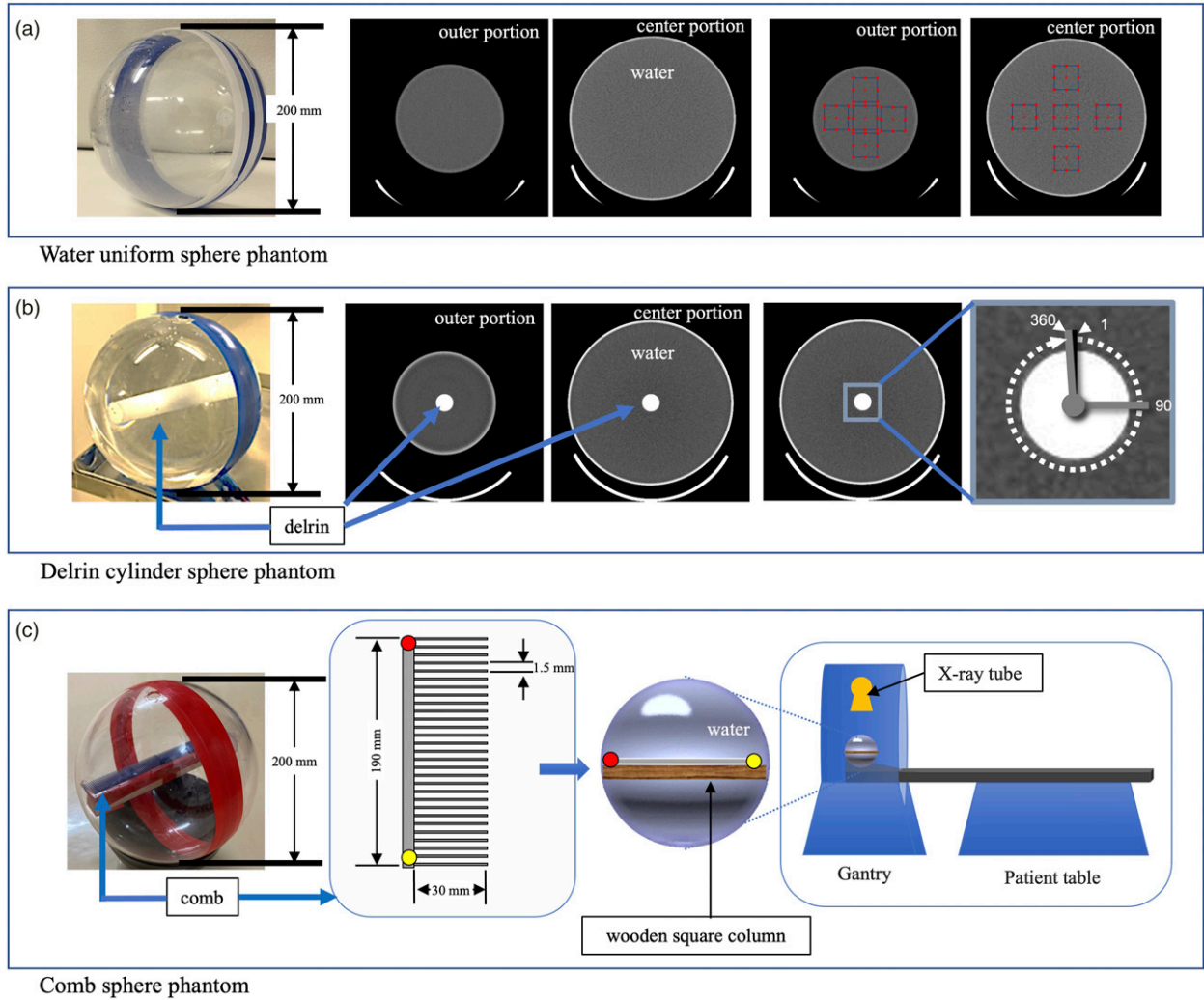


Figure 1. Phantom appearance and measurement position for the image analysis. (a) Water uniform sphere phantom appearance. Phantom center and outer portion of CT images. Measurement position of the CT numbers, image noise, and noise power spectrum. (b) Delrin[®] cylinder sphere phantom appearance and CT images. Measurement position of the TTF to the Delrin[®] cylinder sphere phantom. (c) Comb sphere phantom appearance and schema of the comb. Diagram of the placement of the comb and comb sphere phantoms. The comb was placed in the orientation shown by the red and yellow marks in the placement diagram.

($NPS_{0.2}$) and 0.8 cycle/mm ($NPS_{0.8}$) were compared across all reconstruction algorithms as an index of low-frequency and high-frequency components, respectively.

Task-based transfer function (TTF)

The circular edge method using a Delrin[®] cylinder sphere phantom was used to assess the TTF.^{22–25} TTFs were measured on 29 consecutive axial images (table position: –70 to +70 mm) using ImageJ software. In the first step, 360 concentration profiles (1×33 pixels) were acquired from the center of the Delrin[®] cylinder cross-section across the Delrin[®] edge in 1° increments (Figure 1(b)). In the second step, the edge spread function (ESF) of the Delrin[®] cylinder was obtained from the average of the 360° profiles.

In the third step, TTF was defined as the Fourier transform of the line spread function obtained from the ESF. Finally, the 50% and 10% TTF values were obtained from each slice level, and both values were used to assess the 50% and 10% TTF values uniformity in the longitudinal direction.

Qualitative evaluation of spatial resolution

The spatial resolutions of comb images obtained with different image-reconstruction algorithms using comb sphere phantoms were visually compared. Coronal-plane multiplanar reformation (MPR) images were created with a 0.5-mm slice thickness, 0.5-mm slice interval, and 80-mm FOV along the long axis of the comb.

Statistical analysis

A two-tailed Student's *t*-test was used to compare the maximum and minimum CT numbers for the water uniform sphere phantom, standard deviation of the CT numbers, $NPS_{0.2}$ and $NPS_{0.8}$, and 50% and 10% TTFs. Furthermore, the uniformity (difference between maximum and minimum values) in the longitudinal direction of FBP and other image-reconstruction algorithms was compared. Statistical analyses were performed using a commercially available software (SPSS® Statistic v. 25.0; IBM Corp. New York). A *p*-value of $< .05$ was considered statistically significant.

Results

CT numbers

Figure 2 shows the variations in CT numbers obtained with low- and standard-dose scans in the longitudinal direction (Z-axis). The profile curves of the CT numbers showed higher values at the surrounding center portion and lower values at the surrounding outer portion in all reconstructed images. In all image-reconstruction algorithms, the highest and lowest CT numbers were statistically significant ($p < .001$). However, the CT number for mild and strong MBIR was smaller (at 5.0 HU; maximum: 0.8 HU, minimum: -4.2 HU) than that for FBP (at 6.6 HU; maximum: 1.8 HU, minimum: -4.8 HU) and mild and strong HIR (at 6.8 HU; maximum: 1.8 HU, minimum: -5.1 HU). Significant differences were observed in longitudinal uniformity of low-dose scan (difference between maximum and minimum values) between FBP and mild HIR, between FBP and strong HIR, between FBP and mild MBIR, and between FBP and

strong MBIR (*p*-values of .224, .307, .027, and .014, respectively); for high-dose scans, the corresponding *p*-values were .672, .685, .003, and .002, respectively. The CT numbers showed smaller variation for the MBIR images than for the other reconstruction images in the longitudinal direction. Figure 3 shows the color maps of MPR-sagittal images in the longitudinal direction. The images obtained with mild and strong MBIR were also more visually uniform than those obtained with the other reconstructions algorithms.

Image noise

Figure 4 shows the variations in image noise with low- and standard-dose scans in the longitudinal direction. The strong MBIR image had the lowest image-noise level in the longitudinal direction in the low-dose scan, followed by increasing noise levels for mild MBIR, mild and strong HIR, and FBP. Regarding the standard-dose scan, the image-noise level was also the lowest for strong MBIR, followed by increasing noise levels for strong HIR, mild MBIR, mild HIR, and FBP. The variations in image noise at the center and outer portions were the smallest for strong MBIR and the largest for FBP. In all image-reconstruction algorithms, the highest and lowest image-noise levels were statistically significant ($p < .001$). The low-dose scans showed values of 0.8, 1.7, 2.2, 3.2, and 3.9 HU for strong MBIR, mild MBIR, strong HIR, mild HIR, and FBP, respectively, while the standard-dose scans showed values of 0.8, 1.6, 1.6, 1.7, and 2.0 HU, respectively. Furthermore, the longitudinal uniformity of low- and high-dose scans (difference between maximum and minimum values) differed significantly between FBP and other image-reconstruction algorithms ($p < .001$).

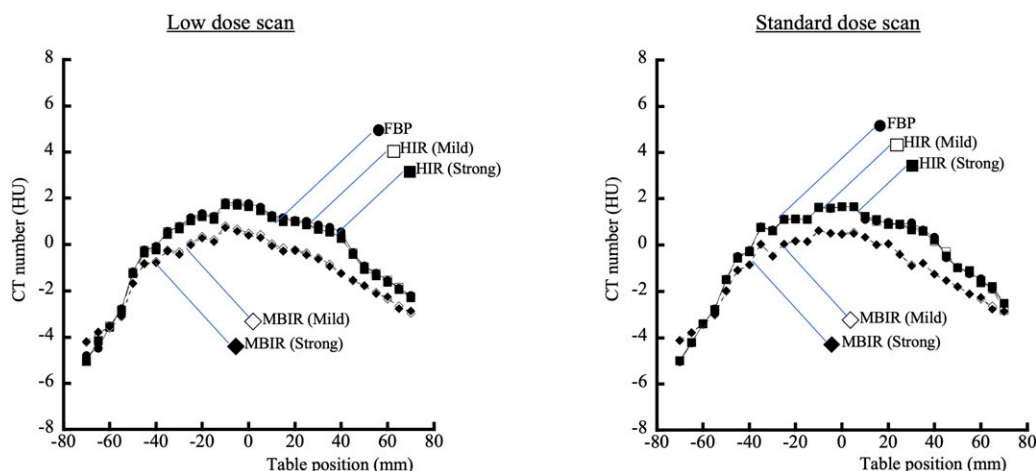


Figure 2. CT numbers for the low-dose and standard-dose scans of the water uniform sphere phantom for each reconstruction algorithm.

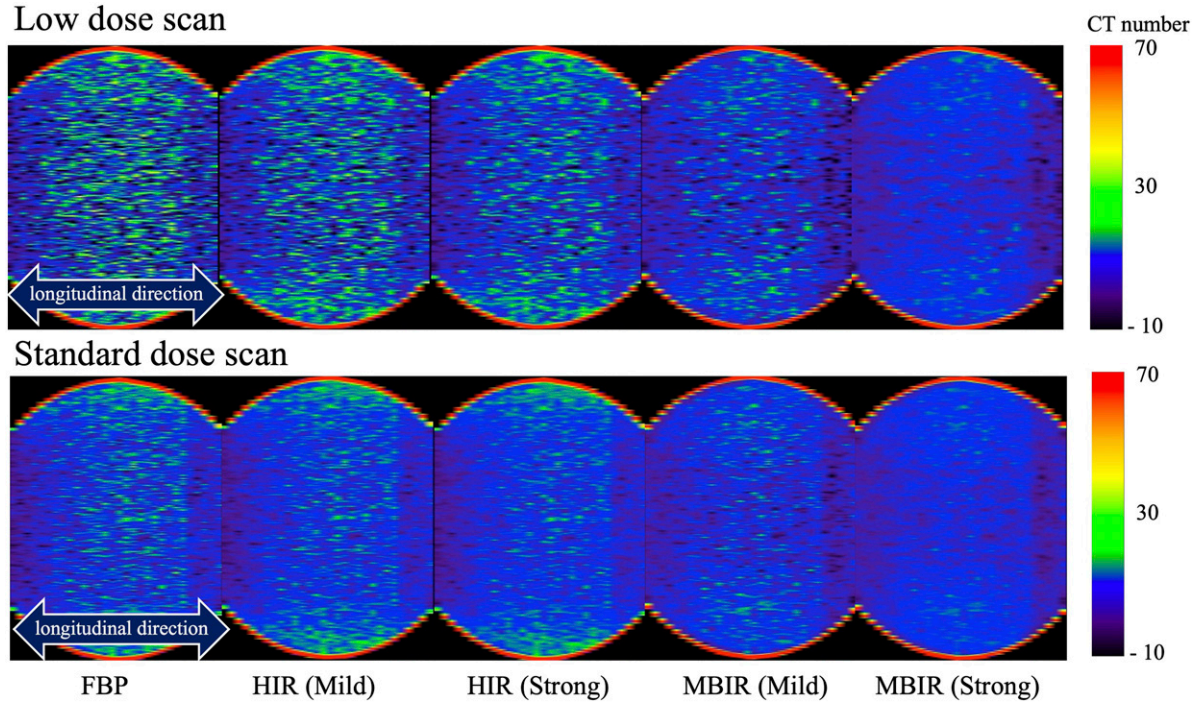


Figure 3. Sagittal images with a CT number color map of the water uniform sphere phantom for each image-reconstruction algorithm. Window width: 80, window level: 30.

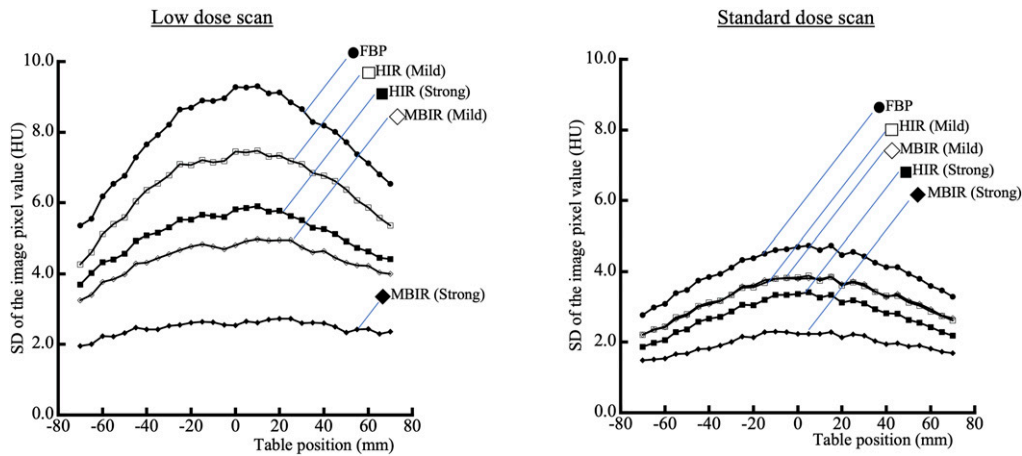


Figure 4. Standard deviation of the CT numbers for low-dose and standard-dose scans of the water uniform sphere phantom for each reconstruction algorithm.

Noise variation of low- and high-frequency components

Table 1 shows the highest and lowest $NPS_{0.2}$ (low-frequency component) values in the longitudinal direction and the differences between them. The $NPS_{0.2}$ for strong MBIR was lower than that for the other reconstruction algorithms in low- and standard-dose scans (Table 1). In addition, the difference between the highest and lowest $NPS_{0.2}$ values for strong MBIR was significantly smaller than that for the other reconstruction

algorithms. For strong MBIR, similar NPS values were obtained regardless of the difference between the low and standard doses. Table 2 shows the highest and lowest $NPS_{0.8}$ (high-frequency component) values in the longitudinal direction and the differences between them. Compared with $NPS_{0.2}$, $NPS_{0.8}$ yielded lower values in all reconstructions. The difference between maximum and minimum values in the longitudinal direction was statistically significant ($p < .001$) in all image-reconstruction algorithms, with strong MBIR exhibiting the lowest values at low- and standard-dose scans.

Table 1. Highest and lowest NPS values for the low-frequency component of 0.2 cycles/mm and the difference between the two values.

Scan technique	Algorithm	IR strength	NPS _{0.2} (HU ² ·mm ²)			p value
			Highest	Lowest	Difference	
Low dose	FBP	—	109.2	23.2	86.0	<.01
	HIR	Mild	98.3	29.6	68.7	<.01
		Strong	82.2	26.8	55.4	<.01
	MBIR	Mild	78.2	27.0	51.2	<.01
		Strong	23.4	11.4	12.0	<.01
Standard dose	FBP	—	35.3	9.0	26.3	<.01
	HIR	Mild	31.7	7.7	24.0	<.01
		Strong	29.3	6.4	22.9	<.01
	MBIR	Mild	29.9	8.4	21.5	<.01
		Strong	15.7	5.5	10.2	<.01

Table 2. Highest and lowest NPS values for the high-frequency component of 0.8 cycles/mm and the difference between the two values.

Scan technique	Algorithm	IR strength	NPS _{0.8} (HU ² ·mm ²)			p value
			Highest	Lowest	Difference	
Low dose	FBP	—	5.37	1.76	3.61	<.01
	HIR	Mild	1.52	0.57	0.95	<.01
		Strong	0.44	0.26	0.17	<.01
	MBIR	Mild	0.27	0.20	0.07	<.01
		Strong	0.08	0.05	0.03	<.01
Standard dose	FBP	—	1.40	0.44	0.95	<.01
	HIR	Mild	0.46	0.13	0.33	<.01
		Strong	0.27	0.08	0.19	<.01
	MBIR	Mild	0.28	0.17	0.11	<.01
		Strong	0.07	0.05	0.03	<.01

Comb image and spatial resolution

Figure 5 shows the MPR-coronal images in each image-reconstruction algorithm at the z-axis center and outer portions of the comb phantom acquired with a low-dose scan. Higher spatial resolution was observed in the outer portion than at the z-axis center portion on mild and strong MBIR and strong HIR. In addition, the TTF outcomes of the low-dose scan of the z-axis center and outer portions were in agreement with visual observations of the MPR-coronal images (Figure 6). Compared with FBP, the TTFs at the z-axis outer portion were markedly improved versus those at the z-axis center portion for strong HIR and mild and strong MBIR. At 50% TTF (Figure 7(a)), higher values were observed for mild and strong MBIR than for the other reconstruction algorithms in the longitudinal direction on low- and standard-dose scans. The outcome tendencies of 10% TTF and 50% TTF were similar (Figure 7(b)). When the longitudinal direction uniformity of FBP was compared to that of other image-reconstruction algorithms, mild HIR for low-dose scan had a 10% TTF *p*-value of .396 and a 50% TTF *p*-value of .2846, whereas mild HIR for high-dose scan had a 10% TTF *p*-value of .067 and a 50% TTF *p*-value of .209, while the others had a *p*-value of < .001.

Discussion

In this study, the effect of image-reconstruction algorithms on the uniformity of image quality in the longitudinal direction was investigated. Single-rotation volume acquisition on head CT was assessed by quantitative and qualitative measurements of CT numbers, image noise, NPS, and spatial resolution of a self-made spherical phantom that simulates the human head.

The tendency of CT numbers to be higher near the center of the phantom for all image-reconstruction algorithms can be attributed to the effect of beam hardening due to the thickness of the subject. Image noise showed the highest uniformity for strong MBIR. In single-rotation volume acquisition with a fixed radiation dose, FBP showed the highest image noise at the z-axis center of the phantom, whereas MBIR reduced the image noise nonlinearly. This finding was supported by the finding that the uniformity of the image noise was proportional to the processing strength of the algorithm. However, this tendency was weaker for the standard-dose scans. In this case, there was already no difference in image noise between the z-axis center and outer vicinities in FBP, suggesting that the intensity of the MBIR image-noise reduction process was low.

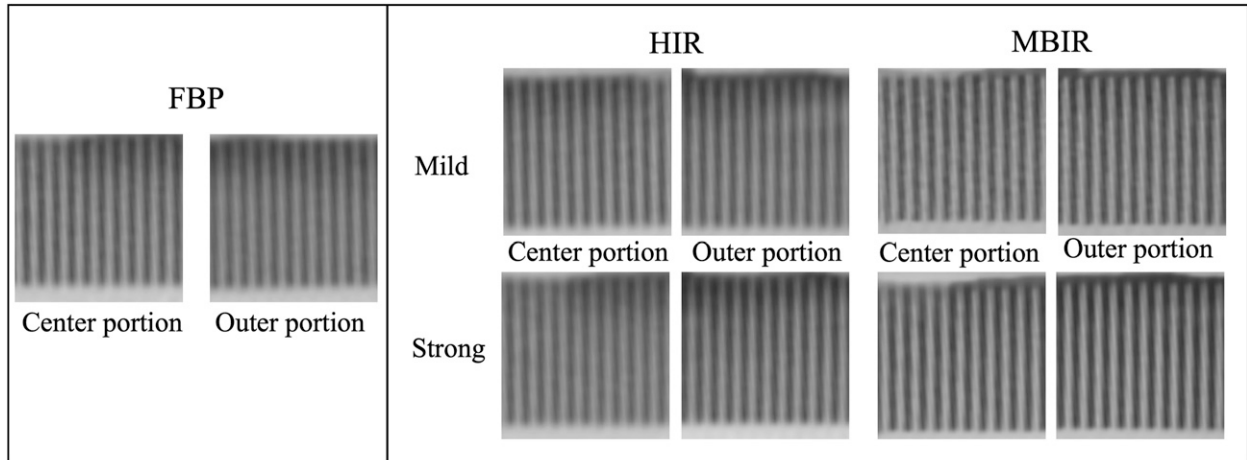


Figure 5. MPR-coronal comb images of the z-axis center and outer portion in low-dose scans with five different reconstruction algorithms.

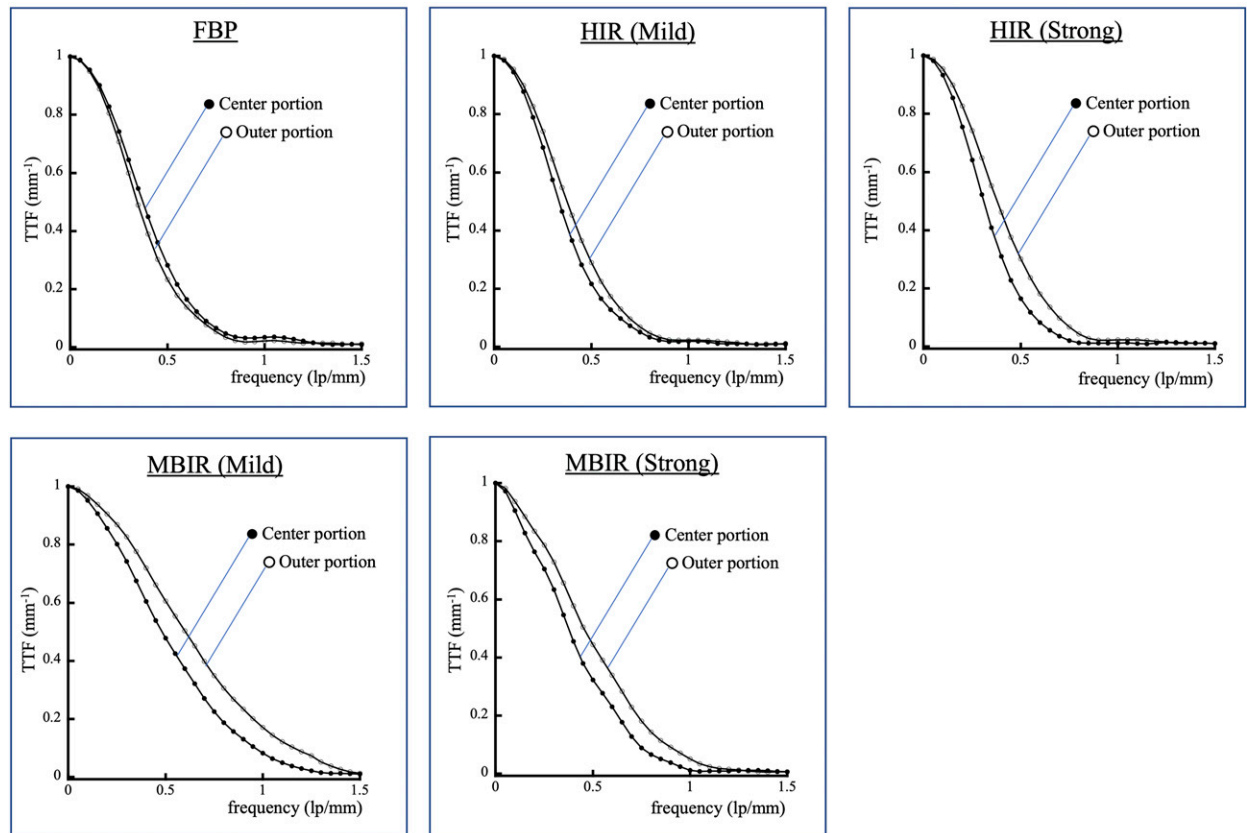


Figure 6. Phantom z-axis center and outer portion TTFs during low-dose scans with five different reconstruction algorithms.

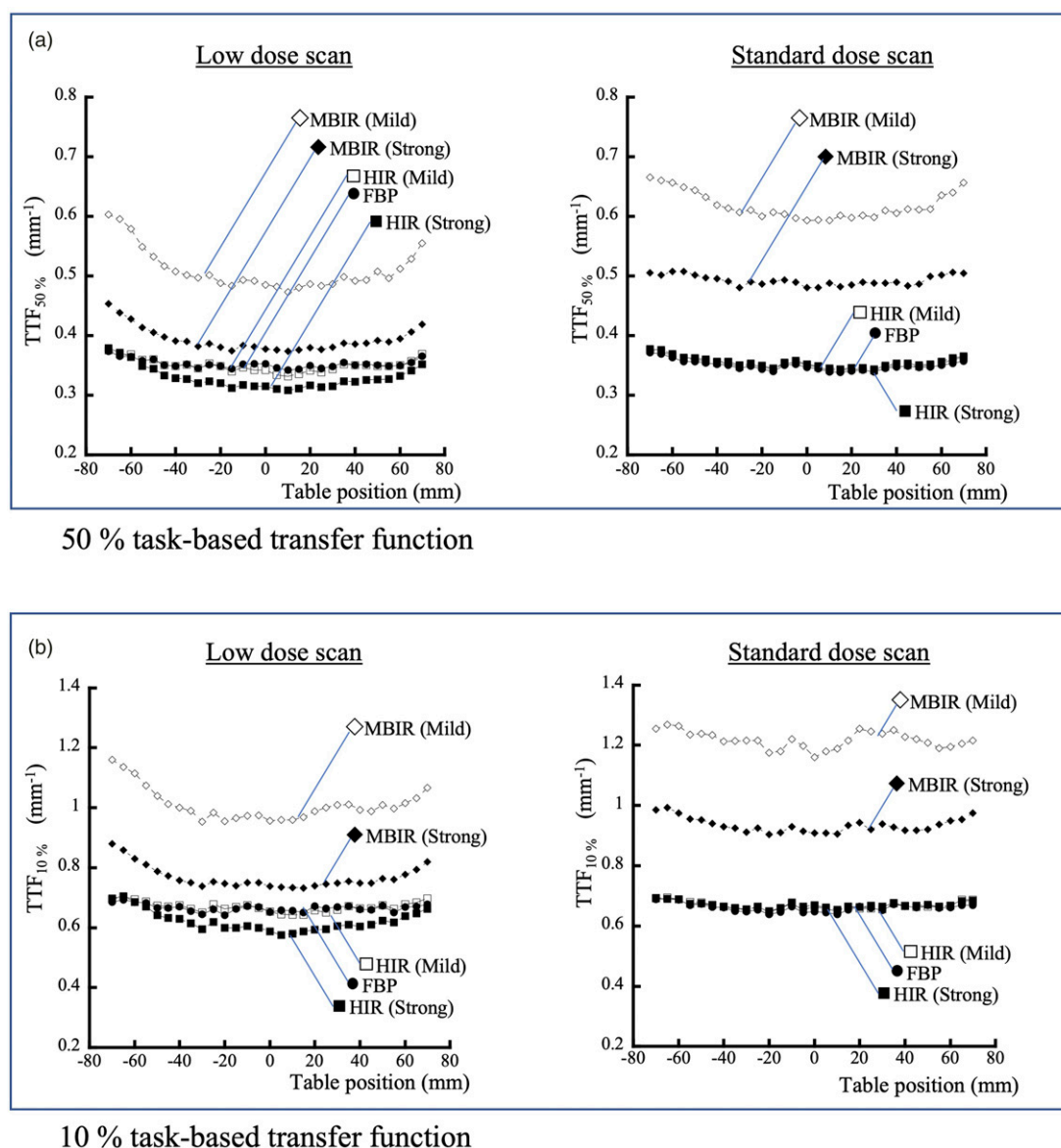


Figure 7. TTFs for the low-dose and standard-dose scans of the Delrin® cylinder sphere phantom for each reconstruction algorithm. (a) Fifty percent TTF. (b) Ten percent TTF.

The $NPS_{0.2}$ also showed that the low-frequency component was much lower for strong MBIR than for the other algorithms. The observation of minute changes in brain parenchymal density, such as in a cerebral infarction, is easily affected by low-frequency noise. Therefore, strong MBIR may be an optimal choice for evaluating brain parenchyma by single-rotation volume head CT. In addition, for all image-reconstruction algorithms, the CT numbers, image noise, and NPS were higher on the anode side than on the cathode side of the X-ray tube. Therefore, we believe that the difference in X-ray intensities caused by the heel effect²⁶ with a wide-volume scan affected the results. Based on these results, when imaging using the entire wide

coverage area, it is necessary to fully consider the effect on image quality due to the spread of the X-ray flux in the longitudinal direction. Furthermore, the impact of the heel effect on clinical imaging, such as lesion detection, must be confirmed.

Image-quality evaluation of IR algorithms requires task-based evaluation methods that account for the structure and target of the desired subject rather than evaluation methods that assume linear behavior.^{21,25} In the quantitative evaluation of spatial resolution, the z -axis TTF was higher in the outer vicinity than in the z -axis center vicinity of the phantom in strong HIR and mild and strong MBIR. This tendency was stronger for low-dose scans than for standard-

dose scans and for MBIR than for HIR. These findings were consistent with the image-noise results. Therefore, the noise-reduction process operated nonlinearly with respect to the amount of image noise, which may have affected the spatial resolution according to the processing strength. Furthermore, on mild and strong MBIR and strong HIR, the spatial resolution was higher along the z-axis outer portion than in the z-axis center portion, which can be attributed to a difference in the transmitted radiation dose caused by the difference in configuration of a thick center and thin outer portions. The TTF results showed that FBP and mild HIR had the highest spatial resolution uniformity in the longitudinal direction. When compared to other image-reconstruction algorithms, MBIR had inferior longitudinal direction uniformity but superior in-plane resolution at all slice positions. Therefore, when considering the overall image quality in clinical practice, choosing MBIR over other reconstruction algorithms may be advantageous. Furthermore, the higher resolution in the outer phantom vicinity is also considered crucial for the evaluation of peripheral vessels in cerebrovascular CT angiography. In this study, the TTF was lower for the low-dose scan than for the standard-dose scan in MBIR. Based on this result, we assume that spatial resolution is affected when excessive dose reduction is corrected by MBIR.

This study had several limitations. First, no skull equivalent was added around the human head phantom, and bone-induced beam hardening was excluded in the reconstructed images. Furthermore, beam hardening by bone may differ from the present results because low-energy X-ray absorption can significantly affect CT numbers in the center and spatial resolution in the periphery. Second, the phantom used in this study was simpler in shape and internal configuration than the human body. Thus, the consistency between our results and clinical examination results must be confirmed in future studies. Third, the effect on spatial resolution was evaluated only in the center of the images, not along the periphery. Finally, we have frequently used mild and strong IR levels on HIR and MBIR in clinical practice; however, we did not verify other IR parameters.

In conclusion, this study evaluated the variations in image-quality characteristics in the longitudinal direction with different image-reconstruction algorithms and strengths in whole-head CT using single-rotation volume scans. MBIR is the optimal image-reconstruction algorithm for single-rotation volume acquisition of spherical subjects owing to high in-plane resolution and the uniformity of CT numbers, image noise, and NPS in the longitudinal direction.

Declaration of Conflicting Interests

The author(s) declared no potential conflicts of interest with respect to the research, authorship, and/or publication of this article.

Funding

The author(s) received no financial support for the research, authorship, and/or publication of this article.

ORCID iDs

Ryo Watanabe  <https://orcid.org/0000-0002-2224-6277>

Yoshinori Funama  <https://orcid.org/0000-0003-1797-9625>

References

1. San Millán Ruiz D, Murphy K, Gailloud P. 320-multidetector row whole-head dynamic subtracted CT angiography and whole-brain CT perfusion before and after carotid artery stenting: technical note. *Eur J Radiol* 2010; 74(3): 413–419.
2. Biswas S, Chandran A, Roughley S, et al. Cerebral CT venography using a 320-MDCT scanner with a time-density curve technique and low volume of contrast agent: comparison with fixed time-delay technique. *American J Roentgenol* 2015; 205(6): 1269–1275.
3. Watanabe Y, Ino K, Yoshikawa K. Discussion about improvement of stability of the scan timing by placing small ROI in cerebral 3D-CTA. *Open J Radiol* 2015; 5(4): 224–234.
4. Shirasaka T, Hiwatashi A, Yamashita K, et al. Optimal scan timing for artery-vein separation at whole-brain CT angiography using a 320-row MDCT volume scanner. *The British J Radiol* 2017; 90(1070): 20160634.
5. Surabhi V, Ashu SB, Arun KG. Diagnostic radiology: pediatric imaging. *Tech Considerat Pediat Imag* 2020.
6. Jeon SK, Choi YH, Cheon JE, et al. Unenhanced 320-row multidetector computed tomography of the brain in children: comparison of image quality and radiation dose among wide-volume, one-shot volume, and helical scan modes. *Pediatr Radiol* 2018; 48(4): 594–601.
7. Siebert E, Diekmann S, Masuhr F, et al. Measurement of cerebral circulation times using dynamic whole-brain CT-angiography: feasibility and initial experience. *Neurol Sci* 2012; 33(4): 741–747.
8. Radon MR, Chandran A, Bhojak M, et al. Radiation dose reduction in 4D cerebral CT angiography by individualized estimation of cerebral circulation time. *American J Neuroradiol* 2016; 37(12): 2189–2194.
9. Hayashida E, Hirai T, Nakamura H, et al. Additive value of 320-section low-dose dynamic volume CT in relation to 3-T MRI for the preoperative evaluation of brain tumors. *Japanese J Radiol* 2016; 34(10): 691–699. DOI: [10.1007/s11604-016-0576-9](https://doi.org/10.1007/s11604-016-0576-9).
10. Gervaise A, Osemont B, Lecocq S, et al. CT image quality improvement using adaptive iterative dose reduction with wide-volume acquisition on 320-detector CT. *European Radiol* 2012; 22(2): 295–301.
11. Komlosi P, Zhang Y, Leiva-Salinas C, et al. Adaptive statistical iterative reconstruction reduces patient radiation dose in neuroradiology CT studies. *Neuroradiol* 2014; 56(3): 187–193.

12. Geyer LL, Schoepf UJ, Meinel FG, et al. State of the art: iterative CT reconstruction techniques. *Radiol* 2015; 276(2): 339–357.
13. Solomon J, Lyu P, Marin D, et al. Noise and spatial resolution properties of a commercially available deep learning-based CT reconstruction algorithm. *Medical Phy* 2020; 47(9): 3961–3971.
14. Urikura A, Ichikawa K, Hara T, et al. Spatial resolution measurement for iterative reconstruction by use of image-averaging techniques in computed tomography. *Radiol Phy Technol* 2014; 7(2): 358–366.
15. Ehman EC, Yu L, Manduca A, et al. Methods for clinical evaluation of noise reduction techniques in abdominopelvic CT. *Rad Graph* 2014; 34(4): 849–862.
16. Fletcher JG, Yu L, Fidler JL, et al. Estimation of observer performance for reduced radiation dose levels in CT. *Academ Radiol* 2017; 24(7): 876–890.
17. Mileto A, Guimaraes LS, McCollough CH, et al. State of the art in abdominal CT: the limits of iterative reconstruction algorithms. *Radiol* 2019; 293(3): 491–503.
18. Racine D, Becce F, Viry A, et al. Task-based characterization of a deep learning image reconstruction and comparison with filtered back-projection and a partial model-based iterative reconstruction in abdominal CT: a phantom study. *Physica Medica, AUGUST* 2020; 76: 28–37.
19. Brady SL, Trout AT, Somasundaram E, et al. Improving image quality and reducing radiation dose for pediatric CT by using deep learning reconstruction. *Radiol* 2021; 298(1): 180–188.
20. Schneider CA, Rasband WS, Eliceiri KW. NIH Image to ImageJ: 25 years of image analysis. *Nat Metho* 2012; 9(7): 671–675.
21. Samei E, Bakalyar D, Boedeker KL, et al. Performance evaluation of computed tomography systems: summary of AAPM task group 233. *Med Phys* 2019; 46(11): 735–756.
22. Greffier J, Hamard A, Pereira F, et al. Image quality and dose reduction opportunity of deep learning image reconstruction algorithm for CT: a phantom study. *European Radiol* 2020; 30(7): 3951–3959.
23. Greffier J, Dabli D, Hamard A, et al. Effect of a new deep learning image reconstruction algorithm for abdominal computed tomography imaging on image quality and dose reduction compared with two iterative reconstruction algorithms: a phantom study. *Quantitati Imag Med Surg* 2022; 12(1): 229–243.
24. Richard S, Husarik DB, Yadava G, et al. Towards task-based assessment of CT performance: system and object MTF across different reconstruction algorithms. *Med Phy* 2012; 39(7): 4115–4122.
25. Mori I, Machida Y. Deriving the modulation transfer function of CT from extremely noisy edge profiles. *Radiol Phy Technol* 2009; 2(1): 22–32.
26. Jiang H. Principles, design, artifacts, and recent advances. Third Edition. Bellingham, WA: Spie Press, 2015, pp. 217–218.